Femtosecond Photoelectron Imaging on Pyrazine: $S_1 \rightarrow T_1$ Intersystem Crossing and Rotational Coherence Transfer

Masaaki Tsubouchi

Chemical Dynamics Laboratory, RIKEN, Wako 351-0198, Japan

Benjamin J. Whitaker

School of Chemistry, University of Leeds, Leeds LS2 9JT, United Kingdom

Toshinori Suzuki*

Chemical Dynamics Laboratory, RIKEN, Wako 351-0198, Japan

Femtosecond time-resolved photoelectron imaging (TR-PEI) is applied to the $(1 + 2')$ resonance-enhanced multiphoton ionization of pyrazine (1,4-diazabenzene) via the S_1 state. The intersystem crossing (ISC) from the S_1 ($n\pi^*$) to the T_1 ($n\pi^*$) state and the ionization dynamics from 3s and $3p_z$ Rydberg states are investigated. Rotational revival features, observed in the time-resolved photoelectron intensities from the T_1 state populated by ISC as well as from the optically prepared S_1 state, are analyzed in detail. The alignment at the rotational revival time in the T_1 state is found to be much smaller than that in the S_1 state. Numerical calculations, using the molecular eigenstate basis and taking account of the angular momentum coupling, to model the transfer of coherence between the S_1 and T_1 states are presented. The calculated time dependence of signal strength and the axis alignment are found to be in excellent agreement with the observed profiles. The diminished alignment in T_1 is explained by the angular momentum coupling mechanism in ISC. Comparison is also made with the rotational coherence transfer in intramolecular vibrational redistribution (IVR). Photoelectron angular distributions (PADs) were also measured in the laboratory frame from spatially aligned ensembles in the 3s and $3p_z$ Rydberg states. The results are qualitatively explained on the basis of the selection rules upon photoionization.

I. Introduction

Time-resolved photoelectron imaging (TR-PEI) is emerging as a powerful means of studying nonadiabatic dynamics in photoexcited molecules. Nonadiabatic transitions are induced, as the result of the breakdown in the Born−Oppenheimer approximation, by rapid vibrational motion at a conical intersection or the seam of crossing between two electronic states and are ubiquitous in the dynamics of polyatomic molecules. TR-PEI launches rovibronic wave packets in the excited electronic states by a pump pulse and projects their evolution on each of the (coupled) electronic states individually and simultaneously to cationic state wave functions by an ionizing probe pulse. The evolving dynamics is observed in a series of photoelectron energy and angular distributions taken at specified pump−probe delays.[1−3] Because the kinetic energy of the photoelectron depends on the binding energy of the molecular orbital being ionized, the signals originating from the different electronic states are generally well resolved in the image. This is in contrast to measurements of photoion yield, effectively the photoionization integral cross section, which are, more often than not, insensitive to the time evolution of the dynamics. TR-PEI interrogates the shape of the electron orbital by observation of the photoelectron angular distribution (PAD). TR-PEI is a variant of more conventional photoelectron spectroscopy with the advantage of measuring the time evolution of both energy and angular distributions simultaneously in a single experiment.[1,3,4]

In previous studies, we applied TR-PEI to investigate the dynamics of $S_1(n\pi^*) \rightarrow T_1(n\pi^*)$ intersystem crossing (ISC) in the azabenzenes: pyrazine,[4−7] pyridine,[8] and pyridazine.[9] These studies usually employed $(1 + 2')$ resonance-enhanced multiphoton ionization (REMPI), although we also studied the ISC dynamics of pyrazine using a $(1 + 1')$ ionization scheme.[1,6]

The $S_1−T_1$ intersystem crossing in pyrazine is the best-known example of the "intermediate case" in the theory of molecular radiationless transitions.[10−12] Strong spin−orbit coupling between any given S_1 state with the moderately dense triplet background states creates a complex energy level structure of molecular eigenstates.[11−13] When a short laser pulse coherently excites these discrete eigenstates, a nonstationary state is created which then rapidly evolves in time. This evolution has previously been monitored by fluorescence from the S_1 state, which exhibits biexponential decay. It is generally believed that the fast component is due to pure dephasing between the component eigenstates and that the slow component is due to depopulation of these eigenstates through deactivation down to S_0.[11−13] However, in the early literature a debate ensued as to whether the observed fast component was due to the predicted dephasing or Rayleigh−Raman light scattering. With the development of ultrafast laser spectroscopy, convincing evidence for the dephasing mechanism was obtained[14] and consistency was found with

the results of high-resolution spectroscopy. (The biexponential decay has also been observed with nanosecond laser excitation, despite the fact that the level density deduced from high-resolution spectroscopy is insufficient to induce ultrafast dephasing for narrow-band laser excitation. It has consequently been suggested that the strong fast component and *J*-dependent fluorescence quantum yield[15] observed with nanosecond lasers are, indeed, due to nonresonant light scattering.[16])

The formation of dark triplet states following ISC has been confirmed by Hillenbrand et al. using nanosecond $(1 + 1')$ pump−probe photoelectron spectroscopy, in which a broad photoelectron distribution characteristic of ionization from the background states populated by ISC from the S_1 0^0 state was observed.[17] Our TR-PEI experiment using a femtosecond laser clearly demonstrated a rapid decay of the ionization component from S_1 and a corresponding growth of that from T_1 with a clear isosbestic point in a series of photoelectron kinetic energy spectra measured with different time delays.[1,4,5] The TR-PEI result obtained with a $(1 + 1')$ REMPI scheme[1] agreed well with the earlier time-unclocked result by Hillenbrand et al.[17]

Our previous work also revealed an important new feature in the ISC dynamics of pyrazine, i.e., rotational wave packet coherences in the bright and dark states were clearly observed in the time-dependent photoelectron intensities and photoelectron angular distributions.[6] The coherent excitation of an ensemble of rotational levels in a given vibronic band was first studied by Zewail, Felker, and co-workers,[18−20] and the method of extracting rotational constants from the coherent transients observed is known as rotational coherence spectroscopy (RCS).[21] In the TR-PEI of pyrazine, however, we observed coherent transients in the bright (S_1) and the dark (T_1) states. As far as we know, there has been no previous investigation of the rotational coherence in the triplet state populated by ISC because of the experimental difficulty in observing these dark states. Interestingly, we found the amplitude of the revival in the T_1 state was much weaker than that in S_1.

The theoretical description of the rotational coherence setup in the optically bright state is well developed.[19,22] However, it is not immediately applicable to the rotational coherent dynamics in the dark states populated by ISC, since ISC induces *J* level mixing in the dark states as explained in section III.B. Figure 1a illustrates how the coherent excitation occurs in the singlet and triplet states. Rotational levels in the S_1 state are coupled to a number of triplet states by spin−orbit interactions. A femtosecond pump pulse coherently excites an ensemble of these eigenstates in the optically bright S_1 state with the oscillator strength carried by the *P*, *Q*, and *R* transitions from S_0, thus creating a wave packet whose time evolution depends on the phase relationship between its components. Because the component zero-order levels in S_1 are vibronically coupled by the spin−orbit interaction to levels in T_1, they are not eigenstates and themselves evolve in time. The result is that the rotational wave packet initially created in a single vibrational level of S_1 is transferred to the coupled vibrational levels in T_1. In section III of this article, we develop analytical expressions to describe the time-dependent observables of a PEI experiment in terms of the molecular eigenstate description and compare these to experimental results in section IV. We show that the molecular eigenstate description accounts for all the features observed in the photoelectron images.

TR-PEI also provides information on the energetics of the resonant intermediate Rydberg states used as "stepping stones" in the REMPI excitation[7,8] and on the ionization dynamics between the ionized electronic orbital and the outgoing photo-
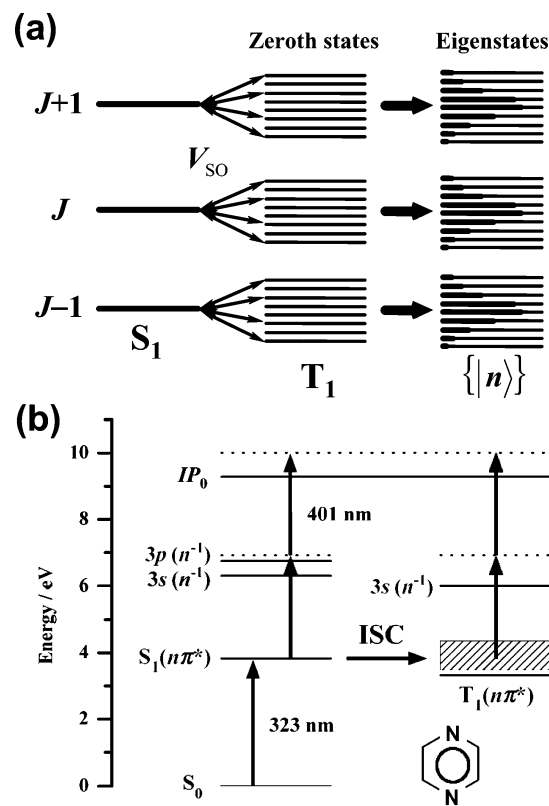

Figure 1. (a) Diagram of the zero-order states and molecular eigenstates coherently excited by a femtosecond pulse. Three rotational states of the S_1 state are excited from the single rotational level of S_0 via *P*, *Q*, and *R* branches. Each rotational state of S_1 is coupled with a manifold of dark T_1 states by the spin−orbit interaction, $\hat{V}_{SO}$, and an ensemble of molecular eigenstates is created. (b) $(1 + 2')$ REMPI scheme of pyrazine. The vertical arrows show the pump and probe pulses.

electron waves.[6,7] This has allowed us to develop a novel Rydberg state spectroscopy based on the vibrational propensity rule between the ionized and the cation states. We have applied this to observe the low-lying Rydberg states of azabenzene molecules[7−9] and to investigate the ionization dynamics.[7] To this aim, the laboratory frame photoelectron angular distributions (LF-PADs) from spatially aligned molecules are recorded and analyzed by considering the relationship between the LF-PADs and the axis alignment initially induced by the pump pulse. We develop this idea in section IV.C.

II. Experimental Section

Figure 1b shows a schematic energy diagram of our pump−probe experiment on pyrazine. A pump pulse centered at 323 nm prepares a rotational wave packet, initially on the ground vibrational state of $S_1(n\pi^*)$. A time-delayed probe pulse centered at 401 nm subsequently interrogates the pumped molecules by resonantly enhanced two-photon ionization via the 3s and 3p Rydberg states.

Approximately 2% pyrazine sample gas was prepared by passing nitrogen over solid pyrazine at room temperature. This sample was continuously expanded into a vacuum chamber at a stagnation pressure of 500 Torr through a 50 μm diameter pinhole. The resulting molecular beam was collimated with a 0.8 mm diameter skimmer and was then introduced into an ionization chamber, where the background pressure (beam on) was ca. 10^{-7} Torr. We chose nitrogen as the carrier gas and set the expansion conditions just described in order to minimize hot bands and cluster formation as measured in the REMPI

spectrum observed by a nanosecond laser. The effective rotational temperature of the pyrazine in the molecular beam was found to be 20 ± 5 K from the observation of the 0_0^0 band contour of the $S_1 \leftarrow S_0$ spectrum.

A 1 kHz pulse train centered at 802 nm was generated by a Nd:YLF-pumped Ti:sapphire regeneratively amplified laser (Coherent, Vitesse and Quantronix, model 527 and Titan). This was split into two equal intensity beams. One beam pumped a commercial optical parametric amplifier (Light Conversion Topas) to generate tunable UV pump light at $\sim$323 nm. The other beam was frequency doubled to generate $\sim$401 nm light in a thin BBO I crystal. In the vacuum chamber, the pump ($\sim$1 μJ) and delayed probe ($\sim$10 μJ) pulses intersected the molecular beam at the center of a stack of ring electrodes which were used to extract the resultant photoelectrons. The cross-correlation time between the pump and probe pulses was determined by the rising edge of the temporal profiles of the total photoelectron intensity to be $\sim$150 fs.

The photoelectrons were accelerated parallel to the molecular beam in a static electric field under velocity mapping focusing conditions.[23] The electrons were detected by a position sensitive imaging detector which consisted of a 40 mm diameter dual microchannel plate (MCP) backed by a P20 phosphor screen. The field-free region of the electron flight path (450 mm) was shielded against stray magnetic fields by a μ-metal tube. Light emission from the phosphor screen was coupled out of the vacuum chamber by a fiber bundle and was recorded by an intensified video rate charge-coupled device (CCD) camera with 768×572 pixels. The total photoelectron current, as monitored by the charge accumulated on the phosphor screen, was also measured. About 50 photoelectrons were created each laser shot. Since we integrated the data for 40 laser shots per video frame, light spots due to different electrons hitting the detector could overlap each other in a single frame. Therefore, the analogue video signal from the CCD was integrated directly without any signal processing such as centeroiding or thresholding.[24] With such a high signal count rate, $\sim$5 $\times$ 10^4 electrons s^{-1}, it was possible to measure each image within several minutes and to record hundreds of photoelectron images with relatively short (500 fs) pump–probe delay steps in a few hours.

III. Theoretical Model

III.A. Representation of Rotational States. Pyrazine belongs to the D_{2h} point group; the z-axis is defined as the axis through the two nitrogen atoms; the x-axis which is perpendicular to the molecular plane is the figure axis of this nearly oblate top molecule.[25] Asymmetry parameters, $\kappa = (2B - A - C)/(A - C)$[26] where A, B, and C are rotational constants, are 0.725 and 0.985 for the ground vibrational states of S_0 and S_1, respectively.[27] In order to simplify our calculations, we approximated pyrazine as an oblate symmetric top, for which the rotational wave function is described as $|JPM\rangle = \sqrt{(2J+1)/8\pi^2}D_{MP}^{J}*(\Omega)$,[28] where P and M are projection quantum numbers of the total angular momentum, J, onto the figure axis and the space-fixed axis, respectively, and $D_{MP}^{J}(\Omega)$ is the rotation matrix element in Euler angles, $\Omega = (\phi,\theta,\chi)$, between the molecular and the space-fixed frames. The transition dipole moment of the $S_1(^1B_{3u}) \leftarrow S_0(^1A_g)$ photoabsorption is parallel to the figure axis, i.e., in the x direction.

The triplet state, with a small spin splitting, is described by Hund's coupling case (b), whereas the singlet state is better represented by case (a). As Hougen has described,[29] the basis sets for these two cases in a near symmetric top molecule are denoted as $|NJKSM\rangle$ and $|JPS\Sigma M\rangle$, where K and Σ are the projection quantum numbers of the rotational (N) and spin (S) angular momenta onto the figure axis, respectively. The latter is essentially an uncoupled basis $|JPM\rangle|S\Sigma\rangle$. The analogy with the diatomic case is such that J, N, K, and P correspond to J, N, Λ, and Ω, where Λ and Ω are the projection quantum numbers of electronic orbital and total angular momentum onto the internuclear axis. Then, the rovibronic state vectors of the S_1 and T_1 states are described as[29]

$$|\Gamma_S;v_S = 0\rangle|J_S P_S M_S\rangle|S_S = 0,\Sigma_S = 0\rangle \quad \text{and}$$

$$|\Gamma_T;v_T^i\rangle|N_T,J_T,K_T,S_T = 1,M_T\rangle \quad (1)$$

respectively, where v represents the vibrational quantum number of ith mode, and Γ includes all other quantum numbers. Here the singlet state is assumed to be the vibrational ground state. The subscripts S and T indicate the S_1 and T_1 states, respectively. The case (b) basis can be expanded in the case (a) bases using[30]

$$|NJK1M\rangle =$$
$$\sum_{P\Sigma} (-1)^{J-1+K}\sqrt{2N+1}\begin{pmatrix} J & 1 & N \\ P & -\Sigma & -K \end{pmatrix}|JPM\rangle|1-\Sigma\rangle \quad (2)$$

Since the $|JPM\rangle$ and $|J-PM\rangle$ states are degenerate, it is in principle necessary to introduce the new basis $|\tau JPM\rangle = [|JPM\rangle + \tau|J-PM\rangle]/\sqrt{2}$ to distinguish the parity, where $P \geq 0$ and $\tau = \pm1$. However, the parity does not affect results in our calculation and is omitted in the following discussion.

III.B. Calculations of Molecular Eigenstates. Each of the S_1 rotational states interacts with a number of T_1 rovibrational states through the spin–orbit coupling operator, $\hat{V}_{SO}$. The eigenstates of the full Hamiltonian including $\hat{V}_{SO}$ are called the molecular eigenstates and are linear combinations of the zero-order S_1 and T_1 states:

$$|n\rangle_{J_S P_S M_S} = a_n^{J_S P_S M_S}|\Gamma_S,0\rangle|0,0\rangle|J_S P_S M_S\rangle +$$
$$\sum_{iN_T K_T} b_n^{iN_T K_T M_S}|\Gamma_T,v_T^i\rangle|N_T J_S K_T 1 M_S\rangle \quad (3)$$

Note that J and M are conserved in the ISC process. The weighting factors, $a_n^{J_S P_S M_S}$ and $b_n^{iN_T K_T M_S}$, and the energies of eigenstates, $E_n^{J_S P_S M_S}$, are given by the solution of the eigen-equation

$$\begin{pmatrix} E_{J_S P_S M_S} & \cdots & V_{J_S P_S M_S}^{iN_T K_T M_S} & \cdots \\ \vdots & \ddots & & 0 \\ V_{J_S P_S M_S}^{iN_T K_T M_S} & & E_{iN_T K_T M_S} & \\ \vdots & 0 & & \ddots \end{pmatrix}\begin{pmatrix} a_n^{J_S P_S M_S} \\ \vdots \\ b_n^{iN_T K_T M_S} \\ \vdots \end{pmatrix} = E_n^{J_S P_S M_S}\begin{pmatrix} a_n^{J_S P_S M_S} \\ \vdots \\ b_n^{iN_T K_T M_S} \\ \vdots \end{pmatrix}. \quad (4)$$

where $E_{J_S P_S M_S} = E_{S_1}^{ele} + E_{J_S P_S M_S}^{rot}$ and $E_{iN_T K_T M_S} = E_{T_1}^{ele} + E_i^{vib} + E_{iN_T K_T M_S}^{rot}$ are the energies of the zero-order S_1 and T_1 rovibronic levels, respectively. The $E_{J_S P_S M_S}$ are easily obtained from the term value and rotational constants of the S_1 0^0 state.[27] However, the $E_{iN_T K_T M_T}$ are not so readily known. Accordingly, we made the following approximations. First, the rotational constants of T_1 were assumed to be the same as those of S_1. This is reasonable since $\bar{B} = (A + B)/2 = 6.116$ GHz in the T_1 0^0 state[31] and 6.097 GHz in the S_1 0^0 state.[27] Second, we assumed that the vibrational states of T_1 were randomly distributed around the S_1 0^0 state with a density of states ρ. Third, the zero-order T_1 rovibronic levels existing in the energy range of $\pm\Delta E$ around the zero-order S_1 rovibronic level were taken into account in the eigenstate calculations.

Using the case (a) basis, the matrix element of the spin−orbit coupling, $V_{J_S P_S M_S}^{i N_T K_T M_S}$, is described:

$$V_{J_S P_S M_S}^{i N_T K_T M_S} = \langle \Gamma_S, v_S = 0 | \langle 0,0 | \langle J_S P_S M_S | \hat{V}_{SO} | N_T J_S K_T 1 M_S \rangle | \Gamma_T, v_T^i \rangle$$

$$= \langle 0 | v_T^i \rangle \sqrt{2N_T + 1} \sum_{\Sigma_T} (-1)^{J_S - 1 + K_T} \begin{pmatrix} J_S & 1 & N_T \\ P_S & \Sigma_T & -K_T \end{pmatrix} \times$$
$$\langle \Gamma_S | \langle 00 | \hat{V}_{SO} | 1 \Sigma_T \rangle | \Gamma_T \rangle \quad (5)$$

The 3j symbol in eq 5 provides the selection rules of $N_T = J_S$, $J_S \pm 1$ and $K_T = P_S + \Sigma_T$. Among the three spin sublevels in the $T_1(^3B_{3u})$ state, only the T_y ($\Sigma_T = \pm 1$) is involved in the spin−orbit coupling.[29,32] Therefore, only six triplet rotational levels ($N_T = J_S$, $J_S \pm 1$ and $K_T = P_S \pm 1$) in each of the coupled triplet vibronic states interact with any given rovibronic state in S_1. In principle, the Franck−Condon factor $\langle 0 | v_T^i \rangle$ depends on the vibrational quantum number in the triplet state, but, for simplicity, we neglect this and approximate all the Franck−Condon factors multiplied by $\langle \Gamma_{S_1} | \langle 00 | \hat{V}_{SO} | 1 \pm 1 \rangle | \Gamma_{T_1} \rangle$ by a single parameter, V.

In order to determine appropriate values for the parameters ρ and V, the population decay from the S_1 state was calculated using[11]

$$I_S^{J_S P_S M_S}(t) = |\langle \Gamma_S, 0 | \langle 0,0 | \langle J_S P_S M_S | \Psi_{J_S P_S M_S}(t;\Omega) \rangle|^2$$

$$\propto \sum_n (a_n^{J_S P_S M_S})^4 + 2 \sum_{n>m} (a_n^{J_S P_S M_S})^2 (a_m^{J_S P_S M_S})^2 \times$$
$$\cos\{(E_n^{J_S P_S M_S} - E_m^{J_S P_S M_S}) t/\hbar\} \quad (6)$$

and the parameters varied so as to reproduce the experimentally observed exponential decay. We discuss this in detail in section IV.B.

III.C. Molecular Axis Alignments in the S_1 and T_1 States. Let us now consider the coherent optical excitation of an ensemble of molecular eigenstates from the ground state. We assume that the oscillator strength is carried only by the singlet state character, and the excitation strength to each $|J_S P_S M_S\rangle$ state from a single rotational state $|J_0 P_0 M_0\rangle$ in the S_0 0^0 state is expressed by $I(J_S P_S M_S; J_0 P_0 M_0)$. Then, the wave function of the nonstationary state created by the laser excitation is

$$\Psi(\Omega; t; J_0 P_0 M_0) \propto$$
$$\sum_{J_S P_S M_S} I(J_S P_S M_S; J_0 P_0 M_0) \sum_n a_n^{J_S P_S M_S} |n\rangle_{J_S P_S M_S} \exp(-i E_n^{J_S P_S M_S} t/\hbar)$$

$$= \sum_{J_S P_S M_S} I(J_S P_S M_S; J_0 P_0 M_0) \times$$
$$\sum_n a_n^{J_S P_S M_S} \left[a_n^{J_S P_S M_S} | \Gamma_S, 0 \rangle | 0,0 \rangle | J_S P_S M_S \rangle + \right.$$
$$\left. \sum_{i N_T K_T} b_n^{i N_T K_T M_S} | \Gamma_T, v_T^i \rangle | N_T J_S K_T 1 M_S \rangle \right] \exp(-i E_n^{J_S P_S M_S} t/\hbar) \quad (7)$$

When linearly polarized light is employed, $I(J_S P_S M_S; J_0 P_0 M_0)$ is more explicitly given by

$$I(J_S P_S M_S; J_0 P_0 M_0) = C(-1)^{M_S - P_S} \sqrt{(2J_0 + 1)(2J_S + 1)} \times$$
$$\begin{pmatrix} J_0 & 1 & J_S \\ P_0 & 0 & -P_S \end{pmatrix} \begin{pmatrix} J_0 & 1 & J_S \\ M_0 & 0 & -M_S \end{pmatrix} \delta_{P_0 P_S} \delta_{M_0 M_S} \quad (8)$$

where C is a constant. The 3j symbols provide the well-known

rotational selection rules, $\Delta J = 0, \pm 1$ and $\Delta P(K) = \Delta M = 0$ for the $S_1 \leftarrow S_0$ transition of pyrazine.

The singlet and triplet components of the nonstationary state are expressed by

$$|\Psi_S(\Omega; t; J_0 P_0 M_0)\rangle =$$
$$\sum_{J_S} |J_S P_0 M_0\rangle | \Gamma_S, 0 \rangle \langle J_S P_0 M_0 | \langle \Gamma_S, 0 | \Psi(\Omega; t; J_0 P_0 M_0) \rangle \quad (9a)$$

and

$$|\Psi_T(\Omega; t; J_0 P_0 M_0)\rangle = \sum_{i J_S N_T K_T} |N_T J_S K_T 1 M_0\rangle | \Gamma_T, v_T^i \rangle \times$$
$$\langle N_T J_S K_T 1 M_0 | \langle \Gamma_T, v_T^i | \Psi(\Omega; t; J_0 P_0 M_0) \rangle \quad (9b)$$

respectively, and the distribution functions of the top axes in the S_1 and T_1 states are (the detail is described in Appendix A)

$$P^S(\theta; t; J_0 P_0 M_0) =$$
$$\iint d\phi \, d\chi \, \langle \Psi_S(\Omega; t; J_0 P_0 M_0) | \Psi_S(\Omega; t; J_0 P_0 M_0) \rangle \quad (10a)$$

for the S_1 state, and

$$P^T(\theta; t; J_0 P_0 M_0) =$$
$$\iint d\phi \, d\chi \, \langle \Psi_T(\Omega; t; J_0 P_0 M_0) | \Psi_T(\Omega; t; J_0 P_0 M_0) \rangle \quad (10b)$$

for T_1. Even in a molecular beam, the thermal rotational distribution in S_0 cannot be neglected. Taking the (incoherent) average over the rotational distribution in S_0, we obtain the final form for the time-dependent axis probability distribution function

$$P^X(\theta; t; T) = \sum_{J_0 P_0 M_0} P^X(\theta; t; J_0 P_0 M_0) \exp(-E_{J_0 P_0 M_0}^{rot}/(k_B T)) \quad (11)$$

where k_B is the Boltzmann constant, T is the rotational temperature in the molecular beam, and $E_{J_0 P_0 M_0}^{rot}$ is the rotational energy of the $|J_0 P_0 M_0\rangle$ state, and X indicates the electronic state.

The axis distribution created by one-photon excitation of an isotropic ensemble of molecules is usually expanded in terms of spherical harmonics

$$P^X(\theta; t; T) = A_{00}^X(t;T) Y_{00}(\theta, \phi) + A_{20}^X(t;T) Y_{20}(\theta, \phi)$$

$$= A_{00}^X(t;T) Y_{00}(\theta, \phi) \left\{ 1 + \frac{A_{20}^X(t;T)}{A_{00}^X(t;T)} \frac{Y_{20}(\theta, \phi)}{Y_{00}(\theta, \phi)} \right\} \quad (12)$$

where A_{20}^X/A_{00}^X ranges from $-1/\sqrt{5}$ ($\sin^2 \theta$ distribution) to $2/\sqrt{5}$ ($\cos^2 \theta$). $A_{00}^X(t;T)$ is essentially the population in the X state, and the axis distribution is characterized by A_{20}^X/A_{00}^X. For the sake of simplicity, we define a normalized alignment parameter $\alpha_{K0}^X(t) = A_{K0}^X(t)/A_{00}^X(t)$, and leave out the temperature T in the following discussion.

When three J states are coherently excited to S_1 from S_0 through a parallel transition according to eq 7, the alignment parameter $\alpha_{20}^S(t = 0)$ in the S_1 state takes the extreme value, $2/\sqrt{5}$ (see Appendix B). As discussed in detail in section IV.B., the corresponding alignment parameter for the triplet component $\alpha_{20}^T(t = 0)$ is reduced.

III.D. Time-Dependent Photoelectron Integral and Differential Cross Sections. In our $(1 + 2')$ REMPI experiment, the population and the molecular axis distribution in the S_1 or T_1 state are probed by two-photon ionization through intermedi-

ate Rydberg states.[6,7] When the polarization of the probe light is linear and is parallel to that of the pump light, the axis distributions created in the Rydberg state are given by $P^X_{Ryd}(\theta;t) = P^X(\theta;t)\cos^2\theta$ and $^1/_2 P^X(\theta;t)\sin^2\theta$ for parallel and perpendicular Rydberg $\leftarrow$ $S_1(T_1)$ transitions, respectively. Since the spin multiplicity is conserved upon photoexcitation, singlet and triplet Rydberg states serve as stepping stones in the REMPI from S_1 and T_1, respectively. The molecular axis distributions created by two-photon excitation from the ground state can be expanded in terms of spherical harmonics

$$P^X_{Ryd}(\theta;t) = A^R_{00}(t)Y_{00}(\theta,\phi) + A^R_{20}(t)Y_{20}(\theta,\phi) + A^R_{40}(t)Y_{40}(\theta,\phi) \tag{13}$$

where X denotes singlet or triplet state. The population and alignment parameters in the Rydberg state are related to those in the S_1 or T_1 state:

$$A^R_{00}(t) = A^X_{00}(t)\{1 + f\alpha^X_{20}(t)/\sqrt{5}\} \tag{13a}$$

$$\alpha^R_{20}(t) = \frac{A^R_{20}(t)}{A^R_{00}(t)} = \frac{7\sqrt{5}\alpha^X_{20}(t) + f\{7 + 2\sqrt{5}\alpha^X_{20}(t)\}}{7\{\sqrt{5} + f\alpha^X_{20}(t)\}} \tag{13b}$$

and

$$\alpha^R_{40}(t) = \frac{A^R_{40}(t)}{A^R_{00}(t)} = \frac{6f\alpha^X_{20}(t)}{7\{\sqrt{5} + f\alpha^X_{20}(t)\}} \tag{13c}$$

Here $\alpha^R_{K0}(t)$ is a normalized value of the alignment parameter and f is a factor of 2 or -1 for the parallel or perpendicular Rydberg $\leftarrow$ S_1/T_1 transitions, respectively. As the time evolution in the Rydberg state is negligible within the femtosecond pulse, the time evolution occurs only in the S_1 and T_1 mixed state prior to ionization by the probe light; i.e., the rotational motion in the Rydberg state during the interaction with a probe laser field can be neglected.

In a cylindrically symmetric system, with the pump and probe laser polarization vectors parallel to each other, the LF-PAD resulting from ionization with three photons can be expanded as[33]

$$I(\theta_k;t) = \sigma(t)[1 + \beta_2(t)P_2(\cos\theta_k) + \beta_4(t)P_4(\cos\theta_k) + \beta_6(t)P_6(\cos\theta_k)] \tag{14}$$

where θ_k is the scattering angle of the photoelectron with respect to the polarization vector of the ionization light, $\sigma(t)$ is the integral cross section, and $P_L(\cos\theta_k)$ is a Legendre polynomial. Since photoionization with the transition dipole either in, or perpendicular to, the molecular plane gives rise to a different composition of partial waves of the outgoing photoelectrons in the molecular frame, the LF-PADs vary with the axis alignment in the Rydberg state at the moment of ionization. Conservation of angular momentum imposes the restrictions that ionization from the Kth-order alignment can only contribute to the $L = K$ or $K \pm 2$th-order anisotropy of the PAD. Thus, the coefficients $\beta_L(t)$ can be expanded in terms of the alignment parameters of the Rydberg state, A^R_{K0}, with expansion coefficients a_{KL0}:[34,35]

$$\beta_L(t) = \frac{\sqrt{2L+1}\displaystyle\sum_{K=L-2\geq 0}^{L+2} a_{KL0}\alpha^R_{K0}(t)}{a_{000} + a_{200}\alpha^R_{20}(t)} \tag{15}$$

Integrating eq 14 over θ_k, we deduce that the time-dependent photoionization intensity (or integral cross section) is proportional to the following quantity

$$I^X(t) = a_{000}A^R_{00}(t) + a_{200}A^R_{20}(t)$$

$$\propto A^X_{00}(t)\left\{\left(1 + \frac{f}{\sqrt{5}}a_{200}\right) + \left(\frac{f}{\sqrt{5}} + \frac{7+2f}{7}a_{200}\right)\alpha^X_{20}(t)\right\} \tag{16}$$

Here, a_{000} is normalized to 1, since the absolute ionization cross section is not obtained in our TR-PEI experiments.

IV. Results and Discussion

IV.A. Time Evolution of Photoelectron Images and the Photoelectron Intensities. Figure 2 shows a series of photoelectron images obtained by ionization via the S_1 $B_{3u}(n\pi^*)$ 0^0 level at the quoted time delays between the pump (323 nm) and probe (401 nm) laser pulses. These are the inverse Abel transforms of the original images and correspond to slices through the 3D photoelectron scattering distributions. The polarization vectors of both pump and probe laser beams are parallel to each other and in the vertical direction in the figure. The original images were integrated for 80 000 laser shots. The structures observed in these images primarily consist of three rings. As assigned in our earlier reports,[4−6] the two outer rings originate from ionization of the optically excited S_1 0^0 state. The innermost ring, which is hardly visible in the early time images, originates from ionization of the T_1 state populated by ISC. The observation of sharp rings indicates that these ionization processes occur with the vibrational propensity rule of $\Delta v = 0$ via intermediate Rydberg states at the resonant energy of $h\nu_{pump} + h\nu_{probe}$ (see Figure 1b). The strong anisotropy clearly visible in the ring structure is further evidence that the ionized states have an electron in an atomic-like orbital.

Figure 3 presents the time-resolved photoelectron kinetic energy distributions (PKEDs) extracted from the images shown in Figure 2. An isosbestic point is clearly seen at 80 meV, which indicates that principally only two interconverting species contribute to the time evolution of the photoelectron spectrum. We therefore attribute the time behavior of the spectrum to ISC from the S_1 to T_1 state. The three major peaks have been already assigned in our previous paper.[7] By conservation of energy

$$PKE = T_R + h\nu_{probe} - IP \tag{17}$$

where PKE is the photoelectron kinetic energy, T_R is the term value of the Rydberg state, $h\nu_{probe}$ is the ionization photon energy, and IP is the ionization potential to which a series of the Rydberg series converges. The peaks A at 640 meV and B at 100 meV were assigned to ionization through the singlet $3p_z(n^{-1})$ ($T_R = 55\ 000$ cm^{-1}) and $3s(n^{-1})$ ($T_R = 50\ 700$ cm^{-1}) Rydberg states, respectively. The peak C at 40 meV was assigned to the triplet $3s(n^{-1})$ ($T_R = 50\ 200$ cm^{-1}) Rydberg state. These states are all members of Rydberg series converging to the lowest cationic state with the (n^{-1}) ion core. A shoulder on the low-energy side ($\sim$550 meV) of peak A is seen in the PKEDs. This may result from ionization via the singlet $3p_x$ state which is located at $T_R = 54\ 400$ cm^{-1}.[27,36]

The time dependence of the photoelectron intensities for each peak (A, B, and C) obtained by the least-squares fitting of the PKEDs to three Lorentzian profiles is shown in Figure 4a. The components A and B, resulting from ionization via the singlet Rydberg states, diminish as a function of time ($\tau = 110 \pm 5$ ps), while the component C from the triplet state grows
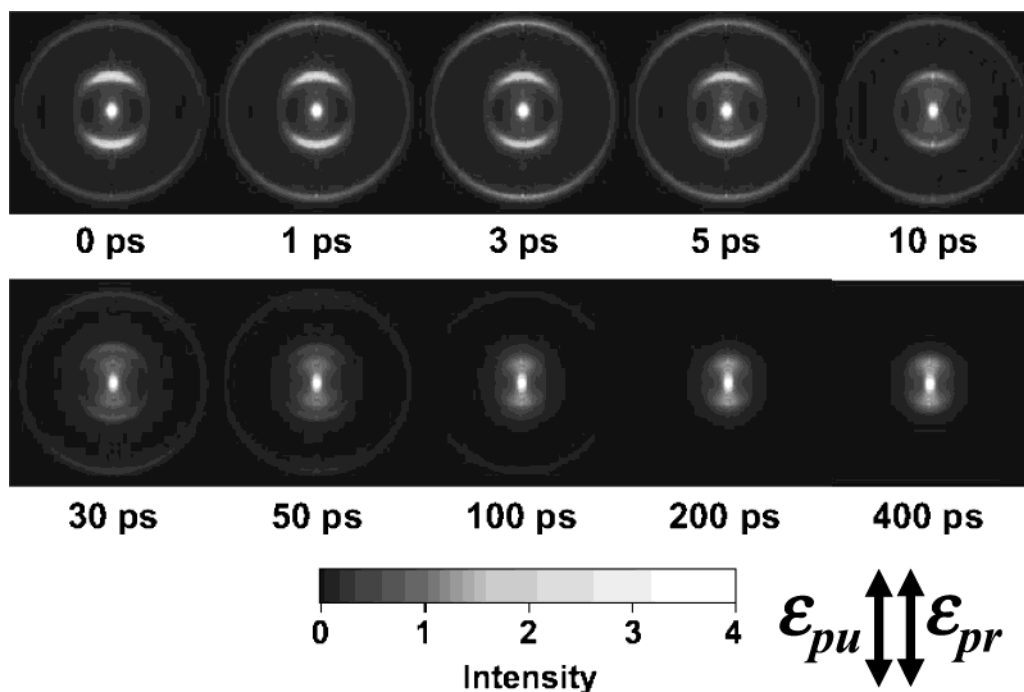
Figure 2. Series of inverse Abel transformed photoelectron images obtained by ionization via the S_1 $B_{3u}(n\pi^*)$ 0^0 level at quoted time delays between the pump (323 nm) and probe (401 nm) lasers. The laser polarizations are both parallel and vertical in the figure. The original images were integrated for 80 000 laser shots.
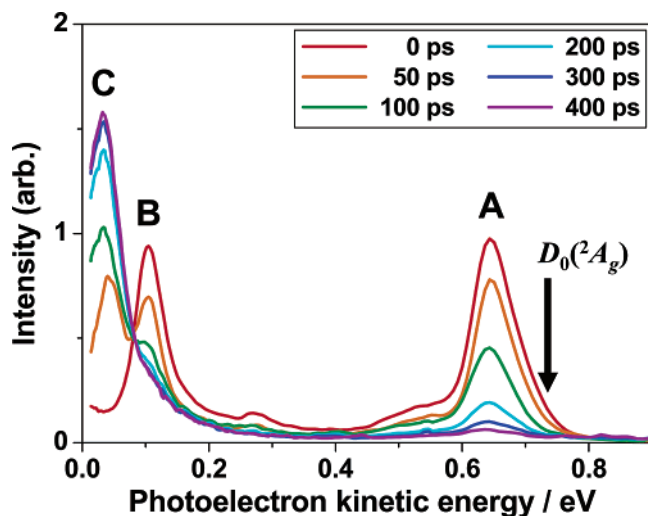

Figure 3. Time evolution of angular integrated photoelectron kinetic energy spectra which were extracted from images shown in Figure 2. D_0 indicates the available energy in the continuum state. The arrows with A, B, and C indicate the three components considered in the analysis.

accordingly. Rapid modulation superimposed on these decay and growth curves is due to time evolution of the rotational wave packet motion with a full revival time period of 82 ps.

The phase of the modulation immediately indicates the direction of the Rydberg ← S_1 transition dipole moment. Close examination of the time dependence of A and B in Figure 4a reveals that at $t = 0$ the intensity is relatively low and high, respectively. Since the figure axes of the excited S_1 pyrazine molecules are aligned parallel to the pump laser polarization at $t = 0$, the result indicates that the transition dipole moments of the Rydberg ← S_1 transitions are, respectively, perpendicular and parallel to the top axis in signals A and B.

With the use of the theoretical framework for RCS developed by Felker and Zewail,[19] the decay profiles can be simulated, as shown by the solid lines in Figure 4a.[6] The spin−orbit coupling
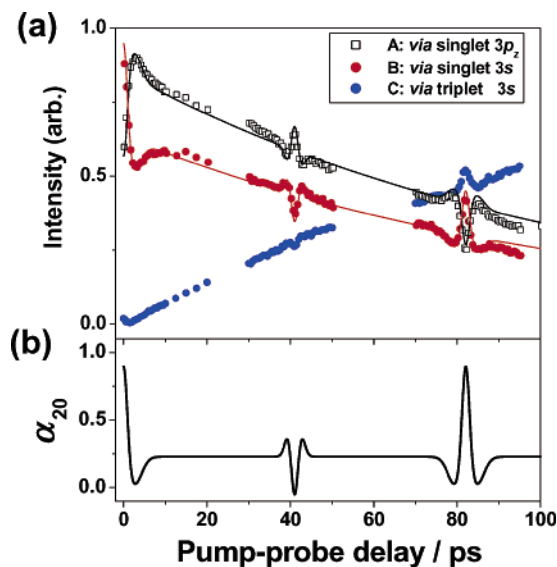

Figure 4. (a) Temporal profiles of the energy-selected photoelectron intensities. A, B, and C indicate the components of the photoelectron kinetic energy distributions shown in Figure 3. The dots are the observed data, and the solid lines are the profiles calculated by eq 16 at the rotational temperature of 20 K. The alignment parameter, A_{20}/A_{00}, in the S_1 state shown in (b) was employed, and the spin−orbit coupling was ignored in the calculation. a_{200} is assumed to be 0.

was ignored in this particular calculation, and only the rotational coherences setup between the zero-order energy levels of the S_1 states were considered. First, the time-dependent molecular axis alignment, $\alpha_{20}^S(t)$, in the S_1 state was calculated for the experimentally determined molecular beam rotational temperature of 20 K, see Figure 4b. With these axis alignment parameters (as discussed below the parameter, a_{200} was set to 0) and eq 16, the observed decay curves can then be simulated for signals A and B, by assuming the transitions to be perpendicular and parallel types, respectively; the only free parameter being the relative ionization cross section for the two
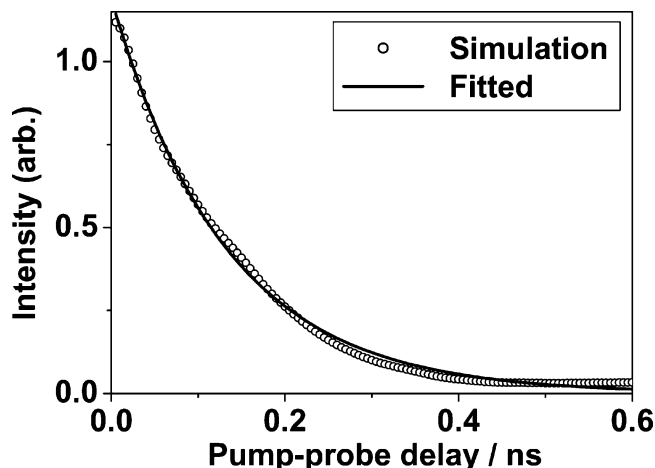
Figure 5. The calculated population decay profile. Open circles are the calculated data with $V = 0.10$ GHz and $\rho = 8$ GHz^{-1}. The solid line is the best-fit single-exponential decay function. The decay constant of $\tau = 132 \pm 5$ ps was obtained.

Figure 6. Time evolution of the molecular axis alignment, α_{20}^X. The solid and dashed lines show the profiles calculated by $\rho = 8$ GHz^{-1} and $V = 0.10$ GHz in the T_1 and S_1 states, respectively. The experimental results for T_1 is also shown as the open circles for comparison. The rotational temperature was set to 20 K.

processes, which was obtained empirically. The calculated profiles agree well with the experimental ones.

Rotational revivals also appear in the signal C, the time profile of the photoelectron intensity from the T_1 state. The revival intervals in C are the same as those in the singlet decay profiles, A and B, but the modulation is much weaker. From eq 16, this indicates that the molecular axis alignment parameter $\alpha_{20}(t)$ is smaller in the T_1 than in the S_1 state, since the modulation depth is directly proportional to it.

IV.B. Molecular Axis Alignment in the Dark State. As mentioned in section III.B, in order to calculate the alignment in the T_1 state, it is first necessary to determine the unknown parameters ρ and V. These parameters were obtained through comparison between the experimental and calculated population decay profiles for the S_1 state using eq 6, which describes the decay after coherent excitation of an ensemble of molecular eigenstates coupled to a single rotational level in S_1.

The S_1 population decay profile calculated with the parameters $V = 0.10$ GHz, $\rho = 8$ GHz^{-1} is shown in Figure 5 as the open circles. Since only the $J_0 = P_0 = 0$ rotational state of S_0 was used in this calculation, the molecules can only be excited via the R branch, and therefore, the rotational coherence effect does not appear in the calculated profile. The profile can be fit rather well by a single-exponential decay function with a time constant of $\tau = 132 \pm 5$ ps. We considered this effective lifetime calculated is close enough to the observed value of 110 ps, so our simulation was performed with these parameters. To obtain this profile we found it crucial to consider the interaction of the pumped singlet state with triplet states over a wide range of energies. Due to the singlet and triplet interactions, the S_1 character $(a_n^{J_S P_S M_S})^2$ distributes over the molecular eigenstates within ± 10 GHz in energy from the zero-order singlet state. Although the amplitude at ± 10 GHz away from the center is less than 1% of that at the center, these weakly coupled states still play an important role in the coherent dynamics. Thus, we took into account the zero-order triplet state around $\Delta E = \pm 10$ GHz from the zero-order singlet state in solving the eigen-equation.

As anticipated from Fermi's Golden rule, similar population decay time constants were obtained with several different sets of the parameters V and ρ. Therefore, it was not possible to determine the parameters V and ρ uniquely from the simulation of the population decay. We chose to take the value of V determined by Siebrand et al. who measured the high-resolution
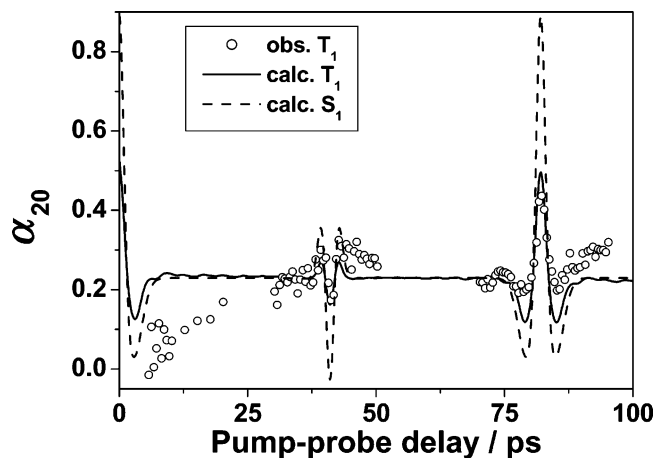
spectra of the molecular eigenstates.[37] We chose to fix V rather than ρ since the density of states estimated spectroscopically may not be accurate because the weakly coupled states are lost in the experimental noise. Using the average experimental value of the coupling strength $V \sim 0.10$ GHz,[37,38] we determined our best estimate for the density of states, $\rho = 8$ GHz^{-1}. Note that although we assumed the spin−orbit coupling between the zeroth-order S_1 and T_1 states to be constant, the values of V determined in the frequency domain study varies over the range from 0.05 to 0.5 GHz.[37,38] In order to investigate the effect of the variation of coupling strength on the time profiles, calculations were also performed for random values of V drawn from a Gaussian distribution with mean 0.10 GHz and standard deviation 0.05 GHz for each zeroth-order triplet state. No significant differences were found between the population profiles derived in this way from those calculated using a constant average value for the coupling strength.

The time evolution of the alignment parameter $\alpha_{20}(t)$ calculated with $V = 0.10$ GHz and $\rho = 8$ GHz^{-1} for the S_1 and T_1 states are shown in Figure 6 as the dashed and solid lines, respectively. The open circles (○) show the experimental values for the T_1 state determined from the temporal profile of the energy-selected photoelectron intensity, C, shown in Figure 4a. To obtain the experimental alignment parameter from the photoelectron intensity, we used the equation $\alpha_{20}^X(t) = \sqrt{5}[I^X(t)/CA_{00}^X(t) - 1]/2$ which was derived from eq 16 by assuming $a_{200} = 0$ and $f = 2$ for the ion ← 3s Rydberg ← T_1 transition. The constant C is proportional to the absolute ionization cross section which was not determined in the present study, therefore, we assumed the value as follows. As shown later, the calculated α_{20}^S and α_{20}^T have the same value ($\alpha_{20}^X = 0.23$) at around a quarter or three-quarters of the revival time, which seems almost invariant with the S−T coupling strength. In the present analysis, we have chosen the constant C so as to make the alignment α_{20}^T to be 0.23 at pump−probe delay times from 25 to 35 ps. The alignment calculated for the S_1 state is the same with the simulation using the zeroth-order S_1 eigenstate shown in Figure 4b, where the spin−orbit coupling was ignored. Gratifyingly, the calculated alignment in the T_1 state at the full revival time when the spin−orbit coupling is included is now much weaker than that in S_1, in excellent agreement with the experimental result (○) extracted from the temporal profile of
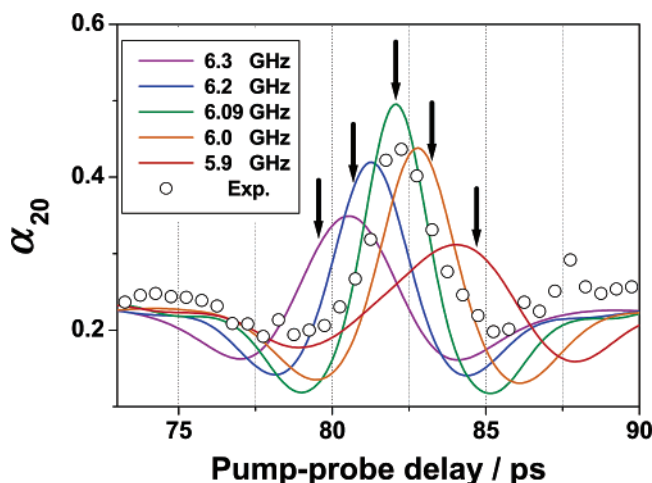
Figure 7. Calculated time evolution of the molecular axis alignment in the T_1 state, α_{20}^T. The rotational constant of the optically bright (S_1) state is $\bar{B} = (A + B)/2 = 6.097$ GHz, while that of the dark (T_1) state is changed from 5.9 to 6.3 GHz. The experimental alignment values in T_1 state is shown as the open circles. The rotational temperature was set to 20 K. The arrows show the revival times, $1/(2\bar{B})$, derived from the rotational constants of T_1.

the energy-selected photoelectron intensity, C, shown in Figure 4a.

In the calculation just described, the rotational constants in the vibrationally excited triplet states were assumed to be the same as those in the S_1 0^0 state. Under this assumption, the calculation reproduced the experimental result very well. However, the known rotational constant of T_1 0^0 state is $\bar{B} = 6.116$ GHz[31] and is slightly different from the 6.097 GHz in the S_1 0^0 state.[27] In alternative calculations, the rotational constants of T_1 0^0 used in the simulation were altered by small amounts. The results are shown in Figure 7. The full revival time in the calculated profiles in the T_1 state is then slightly shifted from 82 ps, and the depth of the revival peak becomes even weaker. This result indicates two facts. The first is that the molecular structure is not largely changed following ISC from S_1 to T_1, since the experimentally observed difference in the revival times was not more than 500 fs between the singlet and triplet states. Since the triplet vibronic states isoenergetic with the singlet have vibrational energies of more than 4000 cm^{-1}, a smaller rotational constant than that of T_1 0^0 may be anticipated. The second is that the TR-PEI has the ability to determine the molecular structure even in the dark state, which is not obtainable with the more commonly used fluorescence detection scheme for the RCS. However, the peak position of the rotational recurrence in the calculated profiles for the T_1 state is not exactly the same as that estimated from the rotational constants of T_1. This is due to the fact that the spin–orbit coupling is not strong enough to create the complete ladder of rotational states in the T_1 state, and the revival structure in the T_1 state is strongly influenced by the rotational ladder in the bright state. Therefore, determination of the rotational constants in the dark states from the observed revival times should be attempted cautiously.

As far as we know, this is the first observation of the rotational wave packet dynamics in the triplet manifold populated by ISC. However, there have been experiments where rotational wave packet dynamics probed in conjunction with IVR[20] and predissociation,[39] and it is interesting to compare our results with these cases. Baskin et al. observed rotational coherence effects in the polarized dispersed fluorescence spectrum of jet-cooled *trans*-stilbene at an excess energy of 1249
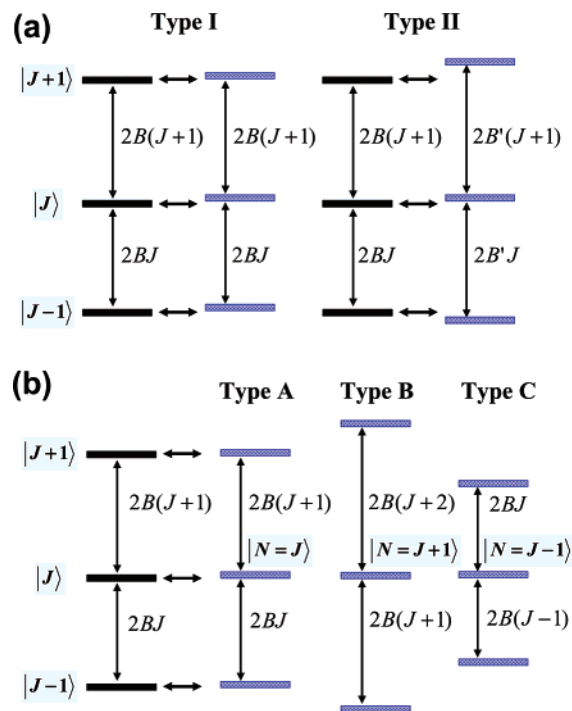

Figure 8. A picture of the rovibrational energy level structure of the interacting optically allowed and dark states in the case of (a) IVR and (b) ISC. (a) In type I, the rotational constants B of the bright state are the same as those of the dark states, while in type II they are different. (b) In ISC, type A, B, and C ladders of the rotational states in the dark states can couple with a single singlet state. Even if the B values of the dark states are the same as that in the bright state, the ladder spacing of type B and C are different from those in the bright state.

cm^{-1}. They measured rotational coherence transients in the emission from the background states populated by IVR with a comparable strength to that in the emission observed by photoexcitation to the zero vibrational level in S_1.[20]

We already know that the optical excitation creates a molecular axis alignment in the optically bright state. If the background vibronic states have the same rotational constants as the bright state, the bright and dark states have the same rotational ladder (type I in Figure 8a). If the coupling between the bright and dark states is governed by the selection rules $\Delta J = \Delta K = 0$, then the mixing strength between the bright and dark states is the same for all the J states. This implies that the excitation probabilities of the $J - 1$, J, and $J + 1$ states in the dark state are exactly the same as those of the bright state, providing maximal alignment. This applies to the *trans*-stilbene case where IVR is induced by anharmonic coupling between the vibrational states. On the other hand, if the rotational constants in the bright and dark states are different, the rotational ladders in the bright and dark states are also different (type II in Figure 8a). This situation results in different excitation probabilities of the $J - 1$, J, and $J + 1$ states in the bright and dark states. Unbalanced excitation of the J states in the dark manifold diminishes the potential alignment. This expectation is numerically demonstrated in Figure 9a. The magnitude of the coherence transients calculated in the type II coupling scheme ($\Delta B = B' - B = -0.2$ GHz) becomes weaker than that in type I, and the revival times are also shifted. Figure 9b shows the coupling strength dependence of the revival peak in dark states populated by IVR. As the coupling strength increases, the peak height of the revival peak increases and approaches the limiting value of $2/\sqrt{5}$. The revival time also gradually shifts from the value close to that in the bright state (82 ps) to the value estimated from the rotational constants of
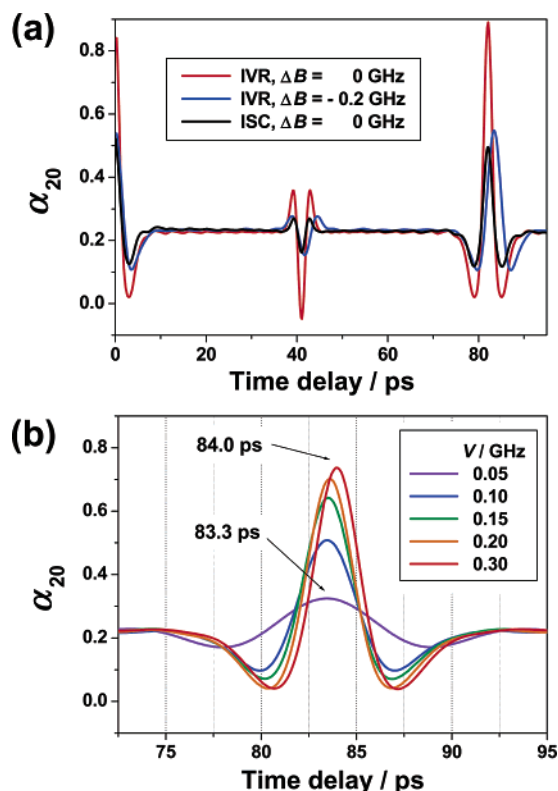
Figure 9. Calculated time evolution of the molecular axis alignment in the optically dark state ($V = 0.10$ GHz and $\rho = 8$ GHz^{-1}). (a) The red and blue lines are the results for IVR with the selection rule $\Delta J = \Delta K = 0$. The rotational constant of the optically bright state was taken to be that for the pyrazine S_1 0^0 state. The rotational constants of the dark states are the same as those of the bright state (the red line) or 0.2 GHz smaller than that state (the blue line). The black line is the calculated alignment in the T_1 state of pyrazine taken from Figure 6. (b) Coupling strength dependence of the revival peak in the dark states populated by IVR. The rotational constants of the dark states are assumed to be 0.2 GHz smaller than that in the bright state.

the dark states (85 ps). This indicates that the rotational revival depends strongly on both the molecular structure and the coupling strength.

Type II coupling can occur in photodissociation or IVR with a large geometrical change. Baskin and Zewail observed the rotational coherence in the photodissociation of the *trans*-stilbene–He complex.[39] The coherent beat measured in the emission from the *trans*-stilbene fragment produced by predissociation of the complex clearly diminished, and at the same time the rotational revival was shifted from that of the complex. Baskin and Zewail,[39] and Blokhin and Gelin[40] have studied this process theoretically. They took into account the change of the rotational angular momentum and the molecular structure and reproduced the reduced rotational coherence observed in the photodissociation process. Pate and co-workers have studied the effect of the "structurally mixed" eigenstates in IVR to interpret their rovibrational spectra.[41] Although they did not consider rotational coherence explicitly, they included the rotational level structure of both the optically bright and dark states in their calculations of the eigenstate spectra and the time evolution of the optically bright state.

In contrast, in the case of pyrazine, even though the rotational constants are essentially the same in both the bright and dark states, the alignment is diminished. This immediately implies that the excitation probability of different J components is influenced by the angular momentum coupling in ISC. As seen from eq 5, the excitation probability of different rotational states
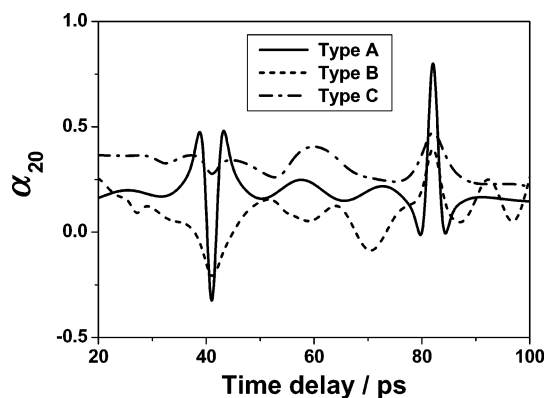

Figure 10. Calculated time evolution of the molecular axis alignment in the optically dark state populated by the spin−orbit coupling ($V = 0.10$ GHz). One optically allowed and one dark state are considered in the calculation. Type A, B, C means the coupling schemes of the singlet−triplet rotational states shown in Figure 9b. The same rotational constants of pyrazine at S_1 0^0 state were assumed for the bright and dark state, and the rotational temperature was 20 K. See the text for more detail.

in the dark state from a single bright rotational state is determined by geometrical factors (the $3j$ symbols). These originate from the transformation from Hund's case (b) to case (a) in eq 2. Since a rotational state of the bright state can couple with the six rotational states ($N = J − 1, J, J + 1, K = P \pm 1$) of the dark state through the spin−orbit interaction, three rotational ladders, which we shall call type A ($N = J$), B ($N = J + 1$), and C ($N = J − 1$), in the dark states must be considered. A schematic picture is shown in Figure 8b. The type B and C ladders are additional sources of quantum beats. Each of the triplet vibronic level contributes to the S−T coupling through only one of these types, and quantum beats between the A, B, and C ladders do not occur due to the orthogonality of the triplet vibronic wave functions. In order to illustrate the beats due to these types we performed a simulation using only one optically bright and one dark vibronic state. We assumed the same rotational constants for both the bright and dark states, and the vibrational energy of the dark state was adjusted so as to make the $J = 2$, $P = 1$ rotational state in S_1 0^0 state isoenergetic to $N = 2$, $K = 0$ (type A), $N = 3$, $K = 0$ (type B), or $N = 1$, $K = 0$ (type C) of the triplet state, respectively. Figure 10 shows the calculated time evolutions of the molecular axis alignment in the optically dark (T_1) state populated by ISC. When both electronic states are coupled via the type A scheme, the rotational wave packet transient in the dark state exhibits the same extreme alignment as the bright state, while the type B and C cases do not. The latter is analogous to type II coupling in IVR. Therefore, the type B and C coupling schemes in ISC play a role similar to the "structurally distorted" background eigenstates in IVR.

We would like to emphasize here the meaning of diminished alignment in our discussion. As seen in Figure 9, the rotational alignment is the same at $t = 0$ and at the full revival time in our simulation. This is natural since the strength of the alignment is encoded in the angular momentum coupling scheme and rotational constants at time $t = 0$ and the rotational dynamics are ballistic in a field-free space. In the literature, it has been reported that the observed alignment sometimes diminishes as time evolves, which seems to be a different phenomenon. The latter is due to the diminishing J-type coherence in the asymmetric top molecule.

One possibility we have not examined in the present work as a source of diminished alignment is that pyrazine becomes

an asymmetric rotor in the triplet state, which might reduce the *J*-type coherent transient. So far there has been no indication of such a large geometrical change in this energy range, and this possibility is not highly likely, although pyrazine might become nonplanar in the higher triplet states.[42]

IV.C. Photoelectron Angular Distributions and Ionization Dynamics. Figure 11a shows the polar plots of time-resolved photoelectron angular distributions for ionization via the singlet 3s, $3p_z$, and triplet 3s Rydberg states at the full rotational wave packet revival time (82 ps). The PAD is more anisotropic for ionization from the 3s state than from the $3p_z$ state. This is in accord with the fact that, in an atomic picture, ionization from an s state provides a pure p wave, whereas the interference between the s and d outgoing waves originating from ionization out of a p state diminishes the anisotropy in the PAD.

As shown in Figure 11a, the observed PADs are well fit by eq 14. The time evolution of the β_2, β_4, and β_6 anisotropy parameters so obtained are shown in Figure 11b. The magnitude of β_6 was found to be negligible in all cases. The anisotropy parameters clearly show periodic variation due to the rotational wave packet dynamics. However, the variation of the anisotropy parameters is rather small (<0.3), indicating that ionization from atomic-like Rydberg orbitals is not strongly affected by the direction of the molecular axis. This result differs from that observed for direct ionization of the S_1 state by (1 + 1′) REMPI in which the PADs were highly sensitive to the molecular axis alignment.[6] The rotational wave packet modulation in the anisotropy parameters of the PADs for ionization via the 3s and $3p_z$ Rydberg states are out of phase with each other. This is the same trend as that observed for the angular integrated photoelectron intensities shown in Figure 4a. The anisotropy parameters from the triplet 3s Rydberg state also depend on the time evolution of the rotational wave packet, although the depth of the coherent spike is smaller than that for ionization via the singlet Rydberg state. Since the electron spin is not expected to significantly affect the ionization dynamics, the depression of the modulation depth is most probably due to the decreased molecular axis alignment in the T_1 state at the full revival time.

We focus now on the PADs obtained by ionization through the singlet Rydberg states. By assuming $a_{200} = 0$, eq 15 can be recast:

$$\beta_2(t) = \sqrt{5}\{a_{020} + a_{220}\alpha_{20}^R(t) + a_{420}\alpha_{40}^R(t)\} \quad (18a)$$

$$\beta_4(t) = 3\{a_{240}\alpha_{20}^R(t) + a_{440}\alpha_{40}^R(t)\} \quad (18b)$$

and

$$\beta_6(t) = \sqrt{13}a_{460}\alpha_{40}^R(t) \quad (18c)$$

Six parameters a_{KL0} are included in eq 18a−c. However, since the axis alignment parameters $\alpha_{20}^R(t)$ and $\alpha_{40}^R(t)$ are not linearly independent, only five parameters can be determined. Parts a and b of Figure 12 show the least-squares fits to β_L for ionization via the singlet 3s and $3p_z$ Rydberg states, respectively. The a_{KL0} values so obtained are listed in Table 1 along with those determined in our previous study,[7] in which the PADs are obtained by one-color (2 + 1) REMPI via the 3s Rydberg state. The parameters determined for the 3s state in this study are slightly different from our previous results.

A few comments should be made on this difference. As Song et al. have discussed,[7] the a_{KL0} parameters of pyrazine can be extracted from (1 + 2′) and (2 + 1) REMPI experiments. The
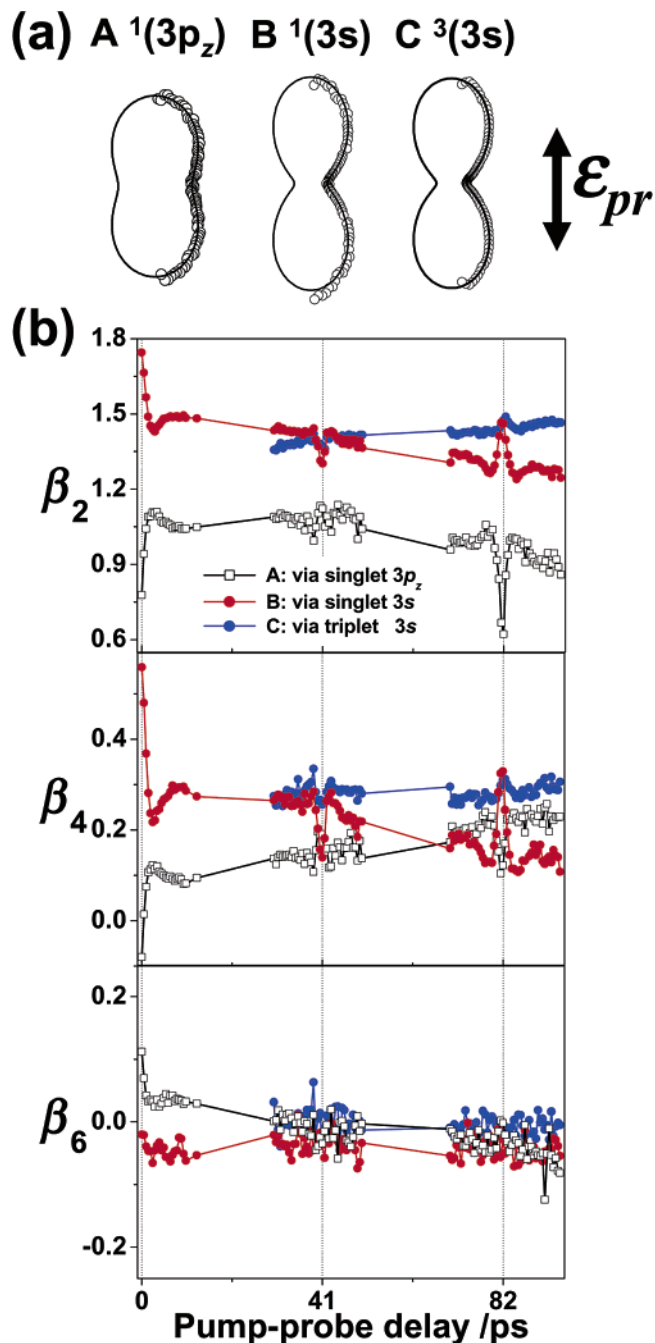

Figure 11. (a) Polar plots of time-resolved photoelectron angular distributions at the pump−probe delay time of 82 ps. The open circles and the lines are the observed data and the nonlinear least-squares fits to eq 14, respectively. A, B, and C indicate the components of the photoelectron kinetic energy distributions shown in Figure 3. The laser polarization is vertical in the figure. (b) Time evolutions of the anisotropy parameters, β_2, β_4, and β_6 of PADs generated by ionization via the singlet $3p_z$, singlet 3s, and the triplet 3s Rydberg states.

reason they utilized these two ionization schemes was that the expected axis alignment was favorably different between them, being $\cos^4\theta$ and $\sin^4\theta$ distributions, respectively. However, they faced the problem that the vibrational energy in the 3s state and the consequent photoelectron kinetic energy were different in the two cases, which could make the analysis inaccurate. The vibrational energies in the 3s state were 5000 cm^{-1} in the (1 + 2′) scheme but 0 cm^{-1} in the (2 + 1) REMPI process via the 0^0 level of the 3s state. The kinetic energy of photoelectrons was, respectively, 0.1 and 0.19 eV in the two cases. The LF-PAD did depend on PKE and/or the vibrational energy in a wide
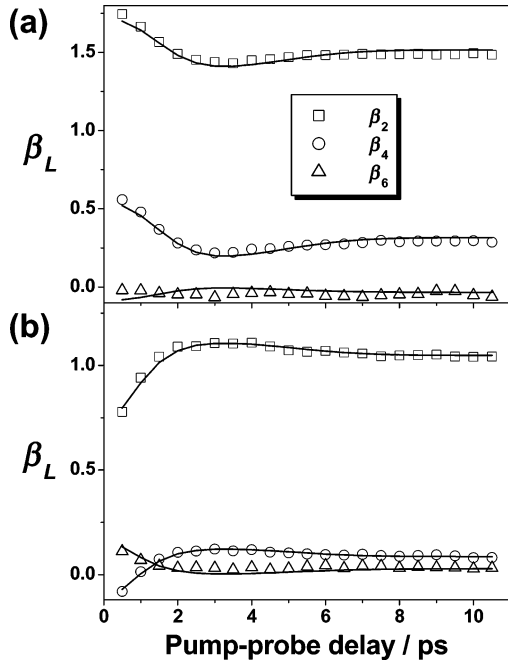
Figure 12. Expanded time profiles of the anisotropy parameters, β_2, β_4, and β_6, of PADs generated by ionization via the singlet (a) 3s and (b) 3p$_z$ Rydberg states. The open dots represent the observed parameters of β_2, β_4, and β_6, respectively. The solid lines are the nonlinear least-squares fits to eq 18.

TABLE 1: Parameters Determined by the Least-Squares Fit of the Time Evolutions of Observed Anisotropy Parameters to Eq 18[a]

	3s (this work)	3s (previous)[7]	3p$_z$ (this work)
a_{000}	$\equiv 1$	$\equiv 1$	$\equiv 1$
a_{200}	0	0	0
a_{020}	$0.27 + 0.89a_{420}$	$0.58 - 0.22a_{420}$	$0.40 + 0.33a_{420}$
a_{220}	$0.39 - 0.99a_{420}$	$0.12 - 0.12a_{420}$	$-0.22 + 0.75a_{420}$
a_{240}	0.06	0.24	-0.09
a_{440}	0.26	-0.38	0.01
a_{460}	-0.06	0	-0.08

[a] Since the basis functions $\alpha_{K0}^R(t)$ are not linearly independent, two parameters a_{020} and a_{220} depend on a_{420}. The errors are within 0.03.

energy range (see Table 2 of ref 7). Although aware of the potential problems, Song et al. determined the a_{KL0} parameters on the assumption that the photoionization dynamics were invariant to PKE and the vibrational energy of the molecule. The energy dependence of photoionization dynamics for near threshold ionization of molecules has not been extensively studied so far, however, in our previous study on the photoionization of NO in the A(3sσ) state, the PKE difference of 0.1 eV had a large effect on the extracted a_{KL0} parameters near the ionization threshold.[43] In the present work, we launched a well-defined rotational wave packet in the S$_1$ state and ionized through the Rydberg state where the alignment in the 3s state was accurately known. The dynamical parameters were extracted from the experimental results obtained for the same pump and probe laser wavelengths measured for different time delays. Thus, the present analysis is expected to be more reliable than the one attempted by Song et al.[7] Recently, we have reported the PADs measured for pyrazine-H4 and -D4 with the probe wavelength of 397 nm, where the results were found to be similar between H4 and D4 but are slightly different from the result obtained with 401 nm reported in the present work.[44] The quantitative analysis of the energy dependence of molecular photoionization dynamics will require more extensive experimental investigation.
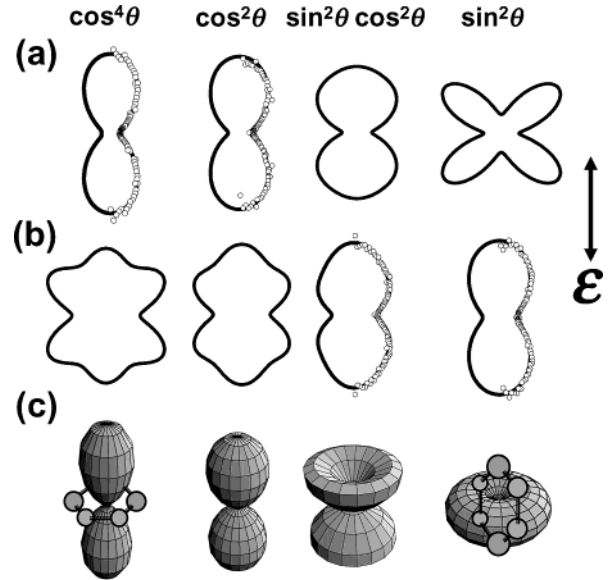

Figure 13. Photoelectron angular distributions calculated for ionization via singlet (a) 3s and (b) 3p$_z$ Rydberg states with different axis alignments. The polarization of the ionization laser is vertical in the figure. The experimental PADs are also shown as the open circles. (c) The molecular axis distributions of pyrazine used in the calculation of the PADs. The most probable alignments of molecules are also indicated in the figures.

The LF-PADs observed in the present work for a weakly (fourth-order) aligned ensemble represent the essential feature of the PADs fixed in the molecule (MF-PADs), since the MF-PADs for ionization via the Rydberg states result from a limited number of partial wave components. From the a_{KL0} parameters in Table 1, LF-PADs were calculated for $\cos^4 \theta$, $\cos^2 \theta$, $\sin^2 \theta \cos^2 \theta$, and $\sin^2 \theta$ axis distributions with respect to the laser polarization as shown in Figure 13a. In the case of molecular axis alignment parallel to the polarization vector ($\cos^4 \theta$ distribution), the parallel transition from the Rydberg to the cation state is mainly induced. In the D_{2h} symmetry group, both the ground state of the cation and the Rydberg 3s state have A$_g$ symmetry, while the Rydberg 3p$_z$ belongs to B$_{1u}$. Since the symmetry of the dipole in the parallel transition with respect to the molecular figure axis is b$_{3u}$, the photoelectron partial waves for ionization via the 3s and 3p$_z$ states should have b$_{3u}$ and b$_{2g}$ symmetry, respectively. When we adopt symmetry adapted spherical harmonics to describe the photoelectron outgoing wave,[35,45] the partial waves belonging to b$_{3u}$ and b$_{2g}$ are described as $X_{l\lambda}^{B_{3u}} = \sqrt{2}\, Y_{l\lambda}(\theta,0) \cos(\lambda\phi)$ with odd l and even λ, and $X_{l\lambda}^{B_{2g}} = i\sqrt{2}\, Y_{l\lambda}(\theta,0) \sin(\lambda\phi)$ with even l and odd λ, respectively, where λ is the projection quantum number of the orbital angular momentum l onto the molecular figure axis. The partial wave function belonging to B$_{3u}$ possesses a high probability density along the x (figure) axis, while that for B$_{2g}$ is similar to a d$_{xz}$ orbital which is vertical to the molecular plane.

If a sufficient number of a_{KL0} could be extracted from the experimentally determined PADs we could fully characterize the ionization dynamics; i.e., deduce the transition dipole moments between the partial waves and the ionized electron orbital and the phase shifts of the partial waves. Unfortunately, the number of a_{KL0} obtained in this study are not enough to determine these parameters and more time-resolved PADs in other polarization or other pump−probe schemes are required.

V. Conclusion

We have applied TR-PEI to $(1 + 2')$ REMPI via the $S_1(n\pi^*)$ and $T_1(n\pi^*)$ states of pyrazine.[4,6,7] The photoionization intensity and photoelectron angular distribution obtained by TR-PEI exhibited periodic modulation with an interval of 82 ps characteristic of rotational wave packet motion. The coherent transient observed for ionization from the T_1 state populated by ISC was much smaller than that from the S_1 state, indicating weaker molecular axis alignment in the triplet manifold. This phenomenon was analyzed through detailed numerical calculations taking into account the angular momentum coupling in ISC. The observed feature of the depressed alignment in the triplet was well reproduced in the simulation. The origin of the diminished alignment in the T_1 state was explained in terms of the excitation probabilities of different J states that are affected by the mismatching of the rotational ladders in the spin−orbit interactions. Similar analysis and comparisons are also made on the rotational coherence transfer in the IVR. Observed laboratory frame PADs from ionization via spatially aligned ensembles in the 3s and $3p_z$ Rydberg states were quantitatively interpreted in the molecular frame.

Appendix A: Distribution Function of the Top Axes

In the present study, it is assumed that the ensemble in the molecular beam is isotropic. The summation over M_0 in eq 10 are performed as

$$P^S(\theta;t;J_0P_0) = \sum_{M_0} P^S(\theta;t;J_0P_0M_0)$$

$$\propto \sum_{J_S'J_S''} (2J_0+1)(2J_S'+1)(2J_S''+1)\begin{pmatrix}J_S' & 1 & J_0 \\ P_0 & 0 & -P_0\end{pmatrix}\begin{pmatrix}J_S'' & 1 & J_0 \\ P_0 & 0 & -P_0\end{pmatrix}\sum_{nm}(a_n^{J_S'P_0})^2(a_m^{J_S''P_0})^2 \times$$

$$\exp\{-i(E_n^{J_S'P_0} - E_m^{J_S''P_0})t/\hbar\}\sum_k \begin{pmatrix}J_0 & 1 & J_S' \\ k & -k+P_0 & -P_0\end{pmatrix}\begin{pmatrix}J_0 & 1 & J_S'' \\ k & -k+P_0 & -P_0\end{pmatrix}|D_{0,-k+P_0}^1(\Omega)|^2 \quad \text{(A1)}$$

and

$$P^T(\theta;t;J_0P_0) = \sum_{M_0} P^T(\theta;t;J_0P_0M_0)$$

$$\propto \sum_{J_S'J_S''} (-1)^{J_S'+J_S''}(2J_0+1)(2J_S'+1)(2J_S''+1)\begin{pmatrix}J_S' & 1 & J_0 \\ P_0 & 0 & -P_0\end{pmatrix}\begin{pmatrix}J_S'' & 1 & J_0 \\ P_0 & 0 & -P_0\end{pmatrix} \times$$

$$\sum_{nm} a_n^{J_S'P_0} a_m^{J_S''P_0} \exp\{-i(E_n^{J_S'P_0} - E_m^{J_S''P_0})t/\hbar\} \sum_{iK_TN_T'N_T''} b_n^{iN_T'K_T} b_m^{iN_T''K_T}\sqrt{(2N_T'+1)(2N_T''+1)} \times$$

$$\sum_{\Sigma_T=\pm1}\begin{pmatrix}J_S' & 1 & N_T' \\ P_0 & \Sigma_T & -K_T\end{pmatrix}\begin{pmatrix}J_S'' & 1 & N_T'' \\ P_0 & \Sigma_T & -K_T\end{pmatrix}\sum_k\begin{pmatrix}J_0 & 1 & J_S' \\ k & -k+P_0 & -P_0\end{pmatrix}\begin{pmatrix}J_0 & 1 & J_S'' \\ k & -k+P_0 & -P_0\end{pmatrix}|D_{0,-k+P_0}^1(\Omega)|^2 \quad \text{(A2)}$$

where k is simply a summation index. The notation M_0 is omitted in the eigenvectors and the eigenvalues.

Appendix B: The Extreme Value of the Alignment Parameter in the S_1 State

Just after the excitation to the S_1 state, the distribution function of the top axis in the S_1 state is described as

$$P^S(\theta;t=0;J_0P_0) = \frac{2\sqrt{\pi}(2J_0+1)Y_{00}(\theta,\phi)}{3}\sum_{J_S'J_S''}(2J_S'+1)(2J_S''+1)\begin{pmatrix}J_S' & 1 & J_0 \\ P_0 & 0 & -P_0\end{pmatrix}\begin{pmatrix}J_S'' & 1 & J_0 \\ P_0 & 0 & -P_0\end{pmatrix}\left[\begin{pmatrix}J_0 & 1 & J_S' \\ P_0 & 0 & -P_0\end{pmatrix}\begin{pmatrix}J_0 & 1 & J_S'' \\ P_0 & 0 & -P_0\end{pmatrix}+\right.$$

$$\begin{pmatrix}J_0 & 1 & J_S' \\ P_0-1 & 1 & -P_0\end{pmatrix}\begin{pmatrix}J_0 & 1 & J_S'' \\ P_0-1 & 1 & -P_0\end{pmatrix}+\begin{pmatrix}J_0 & 1 & J_S' \\ P_0+1 & -1 & -P_0\end{pmatrix}\begin{pmatrix}J_0 & 1 & J_S'' \\ P_0+1 & -1 & -P_0\end{pmatrix}+\frac{1}{\sqrt{5}}\left\{2\begin{pmatrix}J_0 & 1 & J_S' \\ P_0 & 0 & -P_0\end{pmatrix}\begin{pmatrix}J_0 & 1 & J_S'' \\ P_0 & 0 & -P_0\end{pmatrix}-\right.$$

$$\left.\left.\begin{pmatrix}J_0 & 1 & J_S' \\ P_0-1 & 1 & -P_0\end{pmatrix}\begin{pmatrix}J_0 & 1 & J_S'' \\ P_0-1 & 1 & -P_0\end{pmatrix}-\begin{pmatrix}J_0 & 1 & J_S' \\ P_0+1 & -1 & -P_0\end{pmatrix}\begin{pmatrix}J_0 & 1 & J_S'' \\ P_0+1 & -1 & -P_0\end{pmatrix}\right\}\frac{Y_{20}(\theta,\phi)}{Y_{00}(\theta,\phi)}\right] \quad \text{(B1)}$$

In deriving this equation, we assumed that the S_1 and T_1 vibronic wave functions form a complete set, $\sum_n(a_n^{J_S'P_0})^2 = 1$. Considering the coherent excitation of the P, Q, and R branches, we obtain the following identity relations:

$$\sum_{J_S'J_S''}(2J_S'+1)(2J_S''+1)\begin{pmatrix}J_S' & 1 & J_0 \\ P_0 & 0 & -P_0\end{pmatrix}\begin{pmatrix}J_S'' & 1 & J_0 \\ P_0 & 0 & -P_0\end{pmatrix}\begin{pmatrix}J_0 & 1 & J_S' \\ P_0 & 0 & -P_0\end{pmatrix}\begin{pmatrix}J_0 & 1 & J_S'' \\ P_0 & 0 & -P_0\end{pmatrix} = 1 \quad \text{(B2)}$$

$$\sum_{J_S'J_S''} (2J_S' + 1)(2J_S'' + 1)\begin{pmatrix} J_S' & 1 & J_0 \\ P_0 & 0 & -P_0 \end{pmatrix}\begin{pmatrix} J_S'' & 1 & J_0 \\ P_0 & 0 & -P_0 \end{pmatrix}\begin{pmatrix} J_0 & 1 & J_S' \\ P_0 - 1 & 1 & -P_0 \end{pmatrix}\begin{pmatrix} J_0 & 1 & J_S'' \\ P_0 - 1 & 1 & -P_0 \end{pmatrix} = 0 \tag{B3}$$

and

$$\sum_{J_S'J_S''} (2J_S' + 1)(2J_S'' + 1)\begin{pmatrix} J_S' & 1 & J_0 \\ P_0 & 0 & -P_0 \end{pmatrix}\begin{pmatrix} J_S'' & 1 & J_0 \\ P_0 & 0 & -P_0 \end{pmatrix}\begin{pmatrix} J_0 & 1 & J_S' \\ P_0 + 1 & -1 & -P_0 \end{pmatrix}\begin{pmatrix} J_0 & 1 & J_S'' \\ P_0 + 1 & -1 & -P_0 \end{pmatrix} = 0 \tag{B4}$$

Therefore, the distribution function at $t = 0$ is

$$P^S(\theta;t = 0;J_0P_0) = \frac{2\sqrt{\pi}(2J_0 + 1)Y_{00}(\theta,\phi)}{3}\left[1 + \frac{2}{\sqrt{5}}\frac{Y_{20}(\theta,\phi)}{Y_{00}(\theta,\phi)}\right] \tag{B5}$$

and the limited value of the alignment parameter $\alpha_{20}^S(t = 0) = 2/\sqrt{5}$ is easily obtained.

References and Notes

(1) Suzuki, T.; Whitaker, B. J. *Int. Rev. Phys. Chem.* **2001**, *20*, 313.
(2) (a) Neumark, D. M. *Annu. Rev. Phys. Chem.* **2001**, *52*, 255. (b) Seideman, T. *Annu. Rev. Phys. Chem.* **2002**, *53*, 41. (c) Stolow, A. *Annu. Rev. Phys. Chem.* **2003**, *54*, 89. (d) Reid, K. L. *Annu. Rev. Phys. Chem.* **2003**, *54*, 397.
(3) Suzuki, T. Time-Resolved Photoelectron Spectroscopy and Imaging. In *Recent Advances in Chemical Reaction Dynamics*; Yang, X., Liu, K., Eds.; World Scientific: Singapore, 2004; Chapter 12.
(4) Suzuki, T.; Wang, L.; Kohguchi, H. *J. Chem. Phys.* **1999**, *111*, 4859.
(5) Wang, L.; Kohguchi, H.; Suzuki, T. *Faraday Discuss.* **1999**, *113*, 37.
(6) Tsubouchi, M.; Whitaker, B. J.; Wang, L.; Kohguchi, H.; Suzuki, T. *Phys. Rev. Lett.* **2001**, *86*, 4500.
(7) Song, J. K.; Tsubouchi, M.; Suzuki, T. *J. Chem. Phys.* **2001**, *115*, 8810.
(8) Tsubouchi, M.; Suzuki, T. *J. Phys. Chem. A* **2003**, *107*, 10897.
(9) Matsumoto, Y.; Kim, S. K.; Suzuki, T. *J. Chem. Phys.* **2003**, *119*, 300.
(10) (a) Frad, A.; Lahmani, F.; Tramer, A.; Tric, C. *J. Chem. Phys.* **1974**, *60*, 4419. (b) Kommandeur, J.; Majewski, W. A.; Meerts, W. L.; Pratt, D. W. *Annu. Rev. Phys. Chem.* **1987**, *38*, 433.
(11) Lahmani, F.; Tramer, A.; Tric, C. *J. Chem. Phys.* **1974**, *60*, 4431.
(12) Avouris, P.; Gelbart, W. M.; El-Sayed, M. A. *Chem. Rev.* **1977**, *77*, 793.
(13) Bixon, M.; Jortner, J. *J. Chem. Phys.* **1968**, *48*, 715.
(14) (a) McDonald, D. B.; Fleming, G. R.; Rice, S. A. *Chem. Phys.* **1981**, *60*, 335. (b) Yamazaki, I.; Murao, T.; Yamanaka, T.; Yoshihara, K. *Faraday Discuss. Chem. Soc.* **1983**, *75*, 395. (c) Felker, P. M.; Zewail, A. H. *Chem. Phys. Lett.* **1986**, *128*, 221.
(15) (a) Saigusa, H.; Lim, E. C. *Chem. Phys. Lett.* **1982**, *88*, 455. (b) Matsumoto, Y.; Spangler, L. H.; Pratt, D. W. *Chem. Phys. Lett.* **1983**, *98*, 333.
(16) (a) Jonkman, H. Th.; Drabe, K. E.; Kommandeur, J. *Chem. Phys. Lett.* **1985**, *116*, 357. (b) Bitto, H.; Willmott, P. R. *Chem. Phys.* **1992**, *165*, 113. (c) Medvedev, E. S.; Pratt, D. W. *J. Chem. Phys.* **1996**, *105*, 3366.
(17) Hillenbrand, S.; Zhu, L.; Johnson, P. *J. Chem. Phys.* **1990**, *92*, 870.
(18) Felker, P. M.; Baskin, J. S.; Zewail, A. H. *J. Phys. Chem.* **1986**, *90*, 724.
(19) Felker, P. M.; Zewail, A. H. *J. Chem. Phys.* **1987**, *86*, 2460.
(20) Baskin, J. S.; Felker, P. M.; Zewail, A. H. *J. Chem. Phys.* **1987**, *86*, 2483.
(21) (a) Felker, P. M.; Zewail, A. H. Rotational Coherence Phenomena. In *Jet Spectroscopy and Molecular Dynamics*; Hollas, J. M., Phillips, D., Eds.; Blackie Academic & Professional: London, 1995; pp 181. (b) Felker, P. M.; Zewail, A. H. Ultrafast Dynamics of IVR in Molecules and Reactions. In *Jet Spectroscopy and Molecular Dynamics*; Hollas, J. M., Phillips, D., Eds.; Blackie Academic & Professional: London, 1995; pp 222. (c) Riehn, C. *Chem. Phys.* **2002**, *283*, 297.
(22) Myers, A. B.; Hochstrasser, R. M. *J. Chem. Phys.* **1986**, *85*, 6301.
(23) Eppink, A. T. J. B.; Parker, D. H. *Rev. Sci. Instrum.* **1997**, *68*, 3477.
(24) (a) Chang, B. Y.; Hoetzlein, R. C.; Mueller, J. A.; Geiser, J. D.; Houston, P. L. *Rev. Sci. Instrum.* **1998**, *69*, 1665. (b) Cooper, M. J.; Jackson, P. J.; Rogers, L. J.; Orr-Ewing, A. J.; Whitaker, B. J. *J. Chem. Phys.* **1998**, *109*, 4367. (c) Yonekura, N.; Gebauer, C.; Kohguchi, H.; Suzuki, T. *Rev. Sci. Instrum.* **1999**, *70*, 3265.
(25) Innes, K. K.; Byrne, J. P.; Ross, I. G. *J. Mol. Spectrosc.* **1967**, *22*, 125.
(26) Ray, B. S. *Z. Phys.* **1932**, *78*, 74.
(27) Innes, K. K.; Ross, I. G.; Moomaw, W. R. *J. Mol. Spectrosc.* **1988**, *132*, 492.
(28) Zare, R. N. *Angular Momentum: Understanding Spatial Aspects in Chemistry and Physics*; John Wiley & Sons: New York, 1988.
(29) Hougen, J. T. *Can. J. Phys.* **1964**, *42*, 433.
(30) (a) Lefebvre-Brion, H.; Field, R. W. *Perturbations in the Spectra of Diatomic Molecules*; Academic Press: Orlando, 1986. (b) Brown, J.; Carrington, A. *Rotational Spectroscopy of Diatomic Molecules*; Cambridge University Press: Cambridge, 2003.
(31) Holtzclaw, K. W.; Spangler, L. H.; Pratt, D. W. *Chem. Phys. Lett.* **1989**, *161*, 347.
(32) (a) Burland, D. M.; Schmidt, J. *Mol. Phys.* **1971**, *22*, 19. (b) Medvedev, E. S.; Pratt, D. W. *J. Exp. Theor. Phys.* **1998**, *87*, 35.
(33) Yang, C. N. *Phys. Rev.* **1948**, *74*, 764.
(34) Reid, K. L.; Underwood, J. G. *J. Chem. Phys.* **2000**, *112*, 3643.
(35) Underwood, J. G.; Reid, K. L. *J. Chem. Phys.* **2000**, *113*, 1067.
(36) Walker, I. C.; Palmer, M. H. *Chem. Phys.* **1991**, *153*, 169.
(37) Siebrand, W.; Meerts, W. L.; Pratt, D. W. *J. Chem. Phys.* **1989**, *90*, 1313.
(38) van Herpen, W. M.; Meerts, W. L.; Drabe, K. E.; Kommandeur, J. *J. Chem. Phys.* **1987**, *86*, 4396.
(39) Baskin, J. S.; Zewail, A. H. *J. Phys. Chem.* **1994**, *98*, 3337.
(40) Blokhin, A. P.; Gelin, M. F. *Opt. Spectrosc.* **2000**, *88*, 729.
(41) (a) Hudspeth, E.; McWhorter, D. A.; Pate, B. H. *J. Chem. Phys.* **1997**, *107*, 8189. (b) Pate, B. H. *J. Chem. Phys.* **1998**, *109*, 4396. (c) Pate, B. H. *J. Chem. Phys.* **1999**, *110*, 1990. (d) Keske, J.; McWhorter, D. A.; Pate, B. H. *Int. Rev. Phys. Chem.* **2000**, *19*, 363.
(42) (a) Fischer, G. *Can. J. Chem.* **1993**, *71*, 1537. (b) Weber, P.; Reimers, J. R. *J. Phys. Chem. A* **1999**, *103*, 9821.
(43) Tsubouchi, M.; Suzuki, T. Submitted for publication.
(44) Suzuki, T.; Wang, L.; Tsubouchi, M. *J. Phys. Chem. A* **2004**, *108*, 5764.
(45) (a) Chandra, N. *J. Phys. B: At. Mol. Opt. Phys.* **1987**, *20*, 3405. (b) Seideman, T. *Phys. Rev. A* **2001**, *64*, 042504.